UNIVERSITY OF BIRMINGHAM

Research at Birmingham

New traction motor sizing strategy for an HEV/EV based on an overcurrent-tolerant prediction model

Cash, Scott; Xu, Hongming; Zhou, Quan; Olatunbosun, Oluremi; Shaw, Robin; Davis, Sean

Link to publication on Research at Birmingham portal

A New Traction Motor Sizing Strategy for a HEV/EV based on an Overcurrent-tolerant Prediction Model

Scott Cash[1], Quan Zhou[1], Oluremi Olatunbosun[1], Hongming Xu[1*], Sean Davis[2], Robin Shaw[3]

[1] Department of Mechanical Engineering, University of Birmingham, B15 2TT

[2] Textron, Douglas House, Cheltenham, GL51 0AB

[3] Hyperdrive Innovation Ltd, Sunderland, SR5 3NY

*h.m.xu@bham.ac.uk

Abstract: This paper presents a new Hybrid and Electric Vehicle (HEV/EV) traction motor sizing strategy, an overcurrent-tolerant prediction model is used to estimate the dynamic and thermal characteristics of a motor operating in the overcurrent region. This can be used to determine if a prospective traction motor and powertrain configuration is able to fulfil the HEV/EVs target dynamic objectives. Since the prediction model only requires minimal motor torque-speed characteristics, it can be a useful tool during the early development stages of a HEV/EV when the detailed motor parameters used in analytical models cannot be obtained. Allowing the motor to operate in the overcurrent region could downsize the traction motor used in the final HEV/EV design to one that is smaller, easier to package and likely to run in a higher efficiency region. A case study is explored where this sizing strategy is used to convert an aeroplane pushback vehicle into a series HEV and tasked with following a rigorous duty cycle. The feasibility of two HEV configurations are then analysed further. The final HEV design reduces the fuel consumption and engine emissions by up to 52% from the original internal combustion engine powered vehicle.

1. Introduction

The high impact of vehicle emissions on climate change and public health has motivated research into Hybrid and Electric Vehicles (HEV/EV) in recent years [1] [2] [3] [4]. Internal Combustion Engines (ICE) produce a variety of harmful emissions; Carbon Dioxide (CO_2) and Methane (CH_4) are the largest contributors to global climate change; Nitrous Oxides (NOx) have a history of forming smog in densely populated cities; and Particulate Matter (PM) can be carcinogenic [5] [6].

Effective HEV/EV design requires optimising the choice of electrical storage/generation systems and powertrain components to meet the vehicle's target driving range and dynamic performance [7] [8] [9]. The main powertrain components for a series HEV are shown in Fig. 1, these include a traction motor, a genset, and a battery pack [10] [11] [12]. The development process of a HEV/EV must also compromise between other constraints such as price and legislative requirements [13] [14]. Therefore, numerous vehicle iterations may be deliberated before the final design is confirmed.

The temperature of the traction motor and power electronics must remain within safe working limits to prevent overheating and premature component failure. The rate of change in temperature is proportional to the supply current and thus also proportional to the motor's output torque. Motor manufacturers usually offer a series of torque-speed curves (continuous region, overcurrent region 1, overcurrent region 2 etc.) and an efficiency map to represent the characteristics of the motor. Any point within the continuous region can be used for the entire time the motor is in service. The supply current corresponding to the maximum torque within the continuous region is limited to ensure the motor does not overheat. The overcurrent region lets a higher supply current to flow to the motor for a short

period to temporarily produce a larger output torque. The overcurrent region is represented by one or more torque-speed curves, each curve will be assigned a time limit to show how long the peak overcurrent torque can be used before the motor would begin to overheat. Operating in the overcurrent region can be desirable for HEV/EVs because a smaller, cheaper and more efficient motor operating in its overcurrent region could be used to achieve the same output torque as a larger motor confined to its continuous torque-speed region.

Numerous optimisation methods have been explored to assist in the selection of electrical storage/generation and powertrain components. These consider price and component packaging constraints while optimising energy conservation and regeneration [15] [16] [17]. The overcurrent region of the traction motor is not considered in these optimisation methods, the inclusion of which may produce a vehicle with a superior electrical driving range.

The characteristics of a traction motor for HEV/EV simulations can be represented by a series of analytical equations [18] [19] [20] [21]. Numerous temperature estimation methods to monitor the temperature of the motor have been investigated, these remove the need for additional sensors [22] [23] [24] [25] [26]. However, the detailed parameters used to create these models may be difficult to obtain from motor manufacturers and performing a series of experiments to find them is impractical if numerous motors are being considered [27] [28].

This paper aims to estimate the dynamic and thermal characteristics of a motor operating in the overcurrent region using an overcurrent-tolerant prediction model. This control scheme will only use basic motor torque-speed characteristics as they are easily obtained from a motor manufacturer. It would quickly show if a prospective traction motor operating in the overcurrent region and the powertrain configuration would enable the vehicle to achieve its
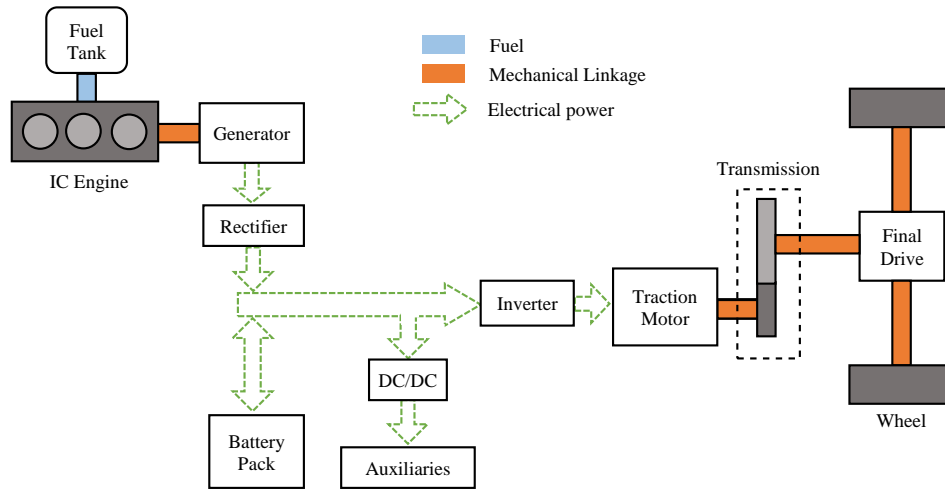
Fig. 1 Typical topology of a single motor series HEV

required dynamic performance. The rate at which the temperature rises and falls will be modelled based on the position of output torque in relation to the continuous and overcurrent torque-speed curves. A case study is presented where this sizing strategy was used to convert an ICE powered aeroplane pushback vehicle into a series HEV. All vehicle and motor models used in this investigation were created and simulated in MATLAB/Simulink. Power management techniques were explored to ensure the battery pack would not overcharge or under-discharge. The battery pack charging scheme also attempts to prolong the life of the genset using manufacturer recommended start-up and cool-down procedures.

This paper is structured as followed; section 2 introduces the overcurrent-tolerant prediction model, section 3 describes the vehicle model used for the aeroplane pushback vehicle with two possible HEV configurations given in section 4.

2. A New Traction Motor Overcurrent-Tolerant Prediction Model

The prediction model can be implemented during the preliminary design stages of a HEV/EV. It can be used to simulate a prospective traction motor within a vehicle model to determine if it would enable the HEV/EV to achieve its target driving objectives. Once an optimal traction motor has been sized, an investigation into more accurate motor control methods and experimental validations can be conducted.

The torque-speed characteristics of a traction motor in this investigation are represented using 2D look-up tables in MATLAB/Simulink (1). The role of the overcurrent-tolerant prediction model is to decide if the continuous C or overcurrent P torque-speed curves should be used in (1). This will output a torque τ for a given motor speed ω_m and accelerator pedal activation level $\alpha \in [0\ 1]$. A control flowchart for the overcurrent-tolerant prediction model is shown in Fig. 2.

The choice of torque-speed curve is dependent on the estimated temperature T (2) of the motor at time t. If the driver of the vehicle model activates the accelerator pedal,

the prediction model initially attempts to access the overcurrent torque-speed curve, where $i = P$ in (1). If $\tau_P(\omega_m) > \widehat{\tau_C}(\omega_m)$, i.e. the output motor torque using the overcurrent curve is larger than the peak continuous torque-speed curve at that motor speed, the overcurrent-tolerant prediction model begins increasing the motor's estimated temperature. The rate of change in temperature is dependent on the position of the output torque $\delta \in [0\ 1]$ using (3) between the peak continuous torque $\widehat{\tau_C}(\omega_m)$ and the peak overcurrent torque $\widehat{\tau_P}(\omega_m)$ at the respective motor speed. The rate of change in temperature is represented by a Temperature Factor TF (4a-b). The integral of TF signifies the overall change in temperature since the beginning of the simulation at time t_0. The temperature increases at a rate according to (4a) in the overcurrent region. For example, if $\widehat{\tau_P}(\omega_m)$ were to be used from an initial temperature $T(t_0) = 0$, then the estimated temperature will reach the upper temperature limit T_{High} over a time period t_{Lim}. If the estimated temperature exceeds T_{High}, the motor will enter a cool-down phase, where $i = C$ in (1). The maximum output torque is restricted to the peak of the continuous

$$\tau_i(\omega_m, \alpha) = \alpha\,\widehat{\tau_i}(\omega_m) \tag{1}$$

Where $i = P, C$

$$T(t) = T(t_0) + \int_{t_0}^{t} TF\, dt \tag{2}$$

Where

$$0 \leq T \leq 100$$

$$\delta(\omega_m) = \frac{\tau_P(\omega_m) - \widehat{\tau_C}(\omega_m)}{\widehat{\tau_C}(\omega_m)} \tag{3}$$

$$TF = \begin{cases} \dfrac{100\,\delta(\omega_m)}{t_{Lim}} & 0 \leq \delta(\omega_m) \leq 1 \tag{4a} \\[4mm] \dfrac{-100}{t_{Stop}} & \delta(\omega_m) < 0 \end{cases} \tag{4b}$$
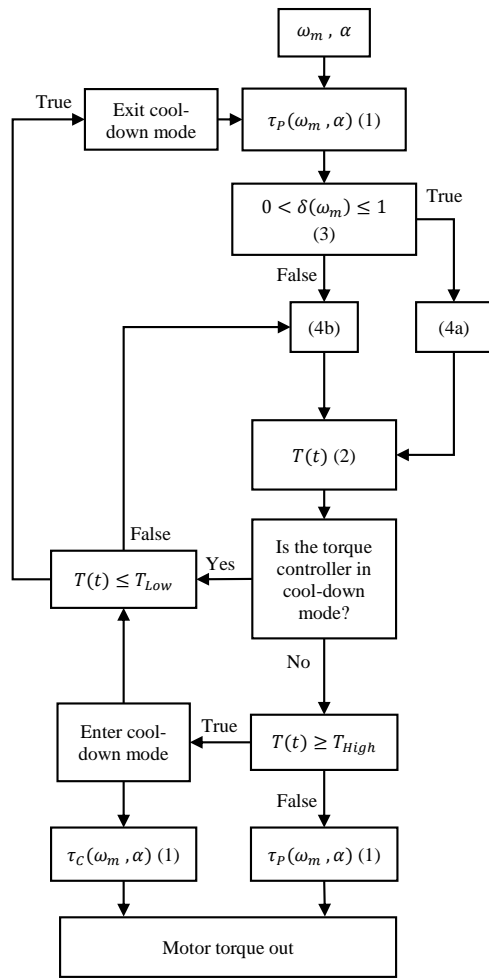
Fig. 2 *Overcurrent-tolerant prediction model torque control flowchart*

region $\widehat{\tau_C}(\omega_m)$ until the estimated temperature reduces to the lower limit T_{Low} over a pre-determined cool-down time t_{stop}. The estimated temperature reduces at a rate according to (4b) during the cool-down phase or whenever the motor is operating in the continuous region. The overcurrent region can be used again once T_{Low} is reached. The time limits t_{Lim} and t_{Stop} accompany the overcurrent torque-speed curves provided by the motor manufacturer. During the cool-down phase, the vehicle's towing and acceleration ability is limited, this is necessary to prevent overheating and premature component failure.

If only a single overcurrent torque-speed curve is given from the motor manufacturer, δ will be a linear function. If numerous overcurrent curves and time limits are provided, δ can be a quadratic function and offer a better view of the motor's thermal characteristics. The overcurrent-tolerant prediction model observes the motor's temperature T as a percentage between T_{High} and T_{Low}. These limits can also

be represented as a percentage, for example T_{High} and T_{Low} are 100% and 50% of the maximum temperature limit respectively. If δ is linear and $\delta = 1$, the motor will output $\widehat{\tau_P}(\omega_m)$ and increase the motor's estimated temperature at a rate where T will reach 100% over the time period t_{Lim}. If $\delta = 0.5$, i.e. the output torque is half way between $\widehat{\tau_C}(\omega_m)$ and $\widehat{\tau_P}(\omega_m)$, the rate of change in temperature will be half that of when $\delta = 1$, the motor can now operate in this region for twice as long. Ideally, the overcurrent region will only be used for a short time period to accelerate the vehicle to a cruising speed where a lower motor torque would be required to maintain a constant steady-state velocity.

3. Traction Motor Sizing for an Aircraft Pushback Vehicle: A Case Study

3.1 Duty Cycle of the Aircraft Pushback vehicle

An aeroplane pushback vehicle is required to move aeroplanes away from airport terminals and occasionally tow them across an airfield for routine maintenance. Therefore, the pushback vehicle must be able to generate a large towing force, but also have a relatively high top speed to travel quickly between pushback operations (~30 kph unloaded). Airport regulations require all pushback vehicles to have the capacity to generate a theoretical minimum tractive force for each aeroplane weight class that the vehicle is registered to move. A HEV aeroplane pushback vehicle must also comply with these regulations. Conventional pushback vehicles use high capacity ICEs as their prime mover with a number of transmission ratios. Between pushback operations, the vehicle might rest for long periods until it is needed again. To avoid any technical difficulties when turning the ICE on (particularly during cold weather), the ICE will remain idling whenever the vehicle is resting. These long idle times significantly increase the total fuel consumption and output emissions over the working day. One major advantage of a HEV pushback vehicle would be that the genset can be turned off during the rest periods as long as there is enough energy stored in the battery pack. Ideally, a series HEV will operate in fully electric mode for a substantial portion of the duty cycle to minimise fuel costs and output emissions.

Duty cycle data was recorded from the pre-existing ICE powered pushback vehicle using a datalogger connected via CAN bus. The datalogger recorded the vehicle's engine speed, output torque, output power, gear selection and longitudinal velocity over several days of normal working operation. From the data collected, a rigorous duty cycle was created and is used to assess the performance of the HEV. The pushback vehicle's duty cycle can be broken down into four major areas as shown in Table 1; low velocity pushback

Table 1 Pushback operation descriptions for the typical ICE vehicle and the HEV equivalent

Operation	No. of operations	M_{Aero} (Tonne)	Target Speed (kph)	Time (s)
Solo	14	0	27	170
Tow	14	250	5	385
Maintenance	2	160	10	1870
Standby	-	0	0	-

operations of heavy aircraft, medium velocity towing operations of medium weight aircraft, high velocity unloaded solo runs, and stationary resting periods. The HEV must have comparable dynamic performance to the ICE counterpart to be a viable product for customers.

The pushback HEV would not be held to conventional passenger vehicle development criteria, i.e. fast 0-60mph acceleration times or to be able to reach motorway cruising speeds. This is because aeroplane manufacturers impose low acceleration limits for towing operations to prevent damage to the landing gear and there are speed limits enforced on working airfields for ground support vehicles.

Suitable powertrain components that would enable the vehicle to achieve the desired duty cycle is investigated first, including; the traction motor torque-speed characteristics, final drive ratio and transmission ratios. The electrical storage and generation components of the HEV can then be explored. The vehicle must have the capacity to complete a full duty cycle using only the energy that can be stored or generated internally. The electrical system requires specifying the minimum capacity and peak output power of the battery pack, as well as the output power of the genset.

3.2 Modelling of the Aeroplane Pushback Vehicle

The torque-speed curve for the 185kW ICE used in the conventional pushback vehicle is given in Appendix 1 in section 8. Fuel consumption and output emissions maps were used to predict the total fuel consumed and emissions produced by the ICE over the duty cycle. Further chassis and powertrain information for the former ICE powered vehicle can be found in Table 2, the same chassis information (vehicle mass, wheel radius etc.) will be used for the HEV.

A fuzzy logic speed controller was used to control the vehicle's speed which attempts to follow the target duty cycle by generating appropriate accelerator $\alpha \in [0\ 1]$ and brake pedal $\beta \in [0\ 1]$ activation levels [18] [29]. The torque generated by an ICE $\tau_{ICE}(\omega_m, \alpha)$ can be found using an equivalent throttle map or (1). A vehicle model was created in MATLAB/Simulink [7] [30] [31].

Table 2 Vehicle parameters of the typical ICE powered pushback vehicle to be converted into a HEV

Parameter	Symbol	Value
ICE only		
Transmission ratios [1,2,3]	N_T	[5.8,2.5,0.98]
Transmission inertia (kg m²) [1,2,3]	I_T	[0.14, 0.1, 0.08]
Final drive ratio	N_{fd}	13
Final drive inertia (kg m²)	I_{Fd}	0.2
Final drive efficiency	η_{Tfd}	0.98
Driveshaft inertia (kg m²)	I_{Fd}	0.17
ICE inertia (kg m²)	I_{ICE}	0.08
ICE and HEV shared		
Vehicle Mass (kg)	M_{Veh}	16000
Coefficient of Drag	C_D	0.8
Frontal Area (m²)	A	6.8
Wheel Radius (m)	r_w	0.575
Coefficient of rolling resistance (%)	f_r	2
Max Brake Force (N)	F_{B-max}	800
Air density (kg m⁻³)	ρ	1.22
Wheel Inertia (kg m²)	I_{Wh}	2.4

The tractive force $F_{Traction}$ (5) requires the gear ratio of the final drive N_{fd}, transmission ratio N_T, their combined efficiency η_{Tfd} and the wheel's rolling radius r_w. This uses the torque generated either by an ICE (where $k = ICE$ in (5)), or from the traction motor as determined by the overcurrent-tolerant prediction model (where $k = C, P$). The rolling resistance $F_{Rolling}$ (6) from the tyres is dependent on the acceleration of gravity g, the coefficient of rolling resistance f_r and the mass of the pushback vehicle M_{Veh}. The mass of the aeroplane M_{Aero} was incorporated into (6) to account for the additional rolling resistance generated by aeroplane. The aerodynamic drag F_{Aero} (7) only requires density of air ρ, the coefficient of aerodynamic drag C_D, frontal area A of the pushback vehicle and the longitudinal velocity U. The brake force F_{Brake} (8) is linearly proportional to the brake pedal activation level and the maximum brake force available on the driving surface F_{B-max}. The effective towing mass of the vehicle M_r (9) due to the rotational inertias of the wheels I_{Wh}, prime mover I_k, final drive I_{Fd} and transmission I_T can then be used to calculate the vehicle's longitudinal acceleration a_x (10). The rotational speed of the prime mover ω_m can then be calculated using (11).

Motor manufacturers often publish an efficiency map $\eta_e(\omega_m, \tau_i)$ for the traction motor, this can be used to find the motor's electrical power consumption P_m (12).

The overcurrent-tolerant prediction model can also be used for the development of HEV/EV passenger vehicles by removing the tow mass of the aeroplane.

$$F_{Traction} = \frac{\tau_k N_{fd} N_T \eta_{Tfd}}{r_w} \tag{5}$$
$$\text{Where } k = ICE, C \text{ or } P$$

$$F_{Rolling} = (M_{Veh} + M_{Aero})gf_r \tag{6}$$

$$F_{Aero} = \frac{1}{2}C_D \rho A U^2 \tag{7}$$

$$F_{Brake} = \beta F_{B-max} \tag{8}$$

$$M_r = \left(I_k N_{fd}^2 + I_T N_{fd}^2 + I_{Fd} N_{fd}^2 + I_{Wh}\right)\frac{1}{r_w{}^2} \tag{9}$$

$$F_{Traction} - F_{Brake} - F_{Aero} - F_{Rolling} = (M_{Veh} + M_{Aero} + M_r)a_x \tag{10}$$

$$\omega_m = \frac{UN_{fd}N_T}{r_w} \tag{11}$$

$$P_m = \frac{\tau_i \omega_m}{\eta_e(\omega_{m,}\tau_i)} \tag{12}$$

3.3 Battery Pack State of Energy and Genset Control

As well as having to power the traction motors, the pushback vehicle must also power its own heating/air-conditioning unit, external warning lights and various other systems on the aeroplane. On the conventional ICE vehicle, these systems are either electrically or hydraulically powered, they will be replaced with fully electrical systems on the HEV. The auxiliary power systems are simplified into a constant load P_{Aux} that will run throughout the duty cycle.

The price of the battery pack grows as its energy storage capacity and peak output power increase. During pushback

and towing operations, the peak power demand from the traction motor is substantially large. A battery pack capable of solely supplying the necessary power for these towing operations would therefore be large and expensive. To reduce the total price of the HEV, a battery pack with a smaller peak output power could be used, but supplement additional power from the genset P_{Gen} to the DC-Link during towing operations. The integral of the power flow to and from the battery pack can be used to estimate the energy remaining within the battery pack J_{Batt} (13) at time t. This can then be used to find the battery pack's State of Energy (SOE).

$$J_{Batt}(t) = J_{Batt}(t_0) + \int_{t_0}^{t} (-(P_m + P_{Aux}) + P_{Gen})\, dt \quad (13)$$

Both the traction motor and auxiliary power systems have priority over the DC-Link power before the battery pack gets charged. The genset is turned on-off to keep the battery pack's SOE within safe upper and lower working limits.

The genset can provide power to the DC-link in one of 3 ways; full power mode, idle mode, and off. A flowchart for the genset control is shown in Fig. 3. During full power mode, the genset will provide full power to the DC-Link and consume fuel at its full rate. During idle mode, the genset will provide no power to the DC-Link, but will consume fuel a fraction of the rated value. For this case study, a value of 10% of the rated fuel is consumed during idle mode. The manufacturer of the genset used in this case study recommended that idle mode should be used for 60 seconds before and after full power mode, this is required to prolong the lifetime of the genset. If the SOE of the battery pack reaches the lower limit during this idling period, the genset will switch to full power mode. This overruling control could adversely affect the genset's lifetime if it occurred frequently, but the more expensive battery pack's sensitivity to under-discharging is a higher priority.

When the genset is off, no power is provided to the DC-Link and no fuel is consumed, the HEV would be operating in full EV mode.

For the HEV to be truly comparable to the ICE counterpart, the SOE of the battery pack should be full at the end of the duty cycle. This would be similar to the ICE vehicle having its fuel tank filled at the end of a working day. Once the final pushback operation has been completed, the genset will enter full power mode (with the necessary start-up phase) and begin charging the battery pack while the HEV returns to the overnight storage area. The genset will turn off once the SOE of the battery pack has reached its upper limit.

4. Feasibility and Efficiency Analysis

The feasible of two powertrain configurations are considered for the final HEV prototype, the parameters for both are given in Table 3. Configuration 1 uses two relatively low torque - high speed in-wheel traction motors with a single gear ratio N_{T-fd}. Configuration 2 uses a single relatively high torque - low speed traction motor with 2 transmission ratios and a final drive.

Table 3 HEV parameters for configuration 1 and configuration 2

Parameter	Config 1	Config 2
Continuous power (kW)	128	245
Continuous torque (Nm)	290	2200
Overcurrent power 60 sec (kW)	200	250
Overcurrent torque 60 sec (Nm)	500	2700
Maximum motor speed (rpm)	8000	3252
$N_{T-fd\,1}$	50	50.28
$N_{T-fd\,2}$	-	28

4.1 Torque Characteristics for Configuration 1

Configuration 1 was developed to fully exploit the traction motors' overcurrent region. A single gear ratio $N_{T-fd\,1}$ was chosen that enabled the HEV to tow the aeroplanes to their target speed for the required time, while also allowing the vehicle to reach its maximum unloaded solo speed.

Fig. 4 shows the traction motor's usage over the torque-speed curves. It can be seen that the overcurrent and constant power regions are fully exploited during the duty cycle. The theoretical temperature profile of the motors in Fig. 5 increases at a greater rate while the HEV is accelerating during a towing operation than when the vehicle reaches its cruising speed. During the maintenance operation, the command torque also enter the overcurrent region to accelerate the vehicle to its target velocity. However, the rate of change in temperature is smaller than the pushback operations and only stays in this region for a short time, the command torque quickly returns to the continuous region to maintain the cruising speed. During solo operations, the command torque remains within the boundaries of the continuous torque region and the motor's temperature does not increase over time.

Fig. 3 Genset control flowchart for the pushback HEV

4.2 Torque Characteristics for Configuration 2

Configuration 2 was developed to meet the minimum tractive force requirements imposed by the airport regulations for the aeroplane weight classes within this duty cycle. A high gear ratio $N_{T-fd\,1}$ will be used during towing and maintenance operations as it achieves the minimum tractive force requirement. A low gear ratio $N_{T-fd\,2}$ was chosen for unloaded solo runs that allows the vehicle to reach its top speed. Fig. 6 shows that the motor usage throughout the duty cycle is within the boundaries of the continuous torque-speed curve. The large headroom between the torque usage and the continuous torque-speed curve shows that the traction motor is oversized for this application. The traction motor would also operates in an inefficient region for a large percentage of the duty cycle. Oversized components also increase the price of the HEV where smaller and cheaper components (Configuration 1) would be sufficient.

4.3 Performance Characteristics for Configurations 1 and 2

Because both HEV configurations accurately follow the target duty cycle, the peak power requirement for both vehicles are similar enough that they can use the same battery pack and genset with parameters given in Table 4.

Fig. 7-Fig. 8 show the SOE of the battery pack, vehicle velocity and the genset operation for Configuration 1 and Configuration 2 respectively over the duty cycle. The mass of the aeroplanes being towed throughout the duty cycle can be found by comparing the HEV velocity in Fig. 7-Fig. 8 against the duty cycle operations in Table 1. The two vehicle configurations are able to follow the target duty cycle with minimal velocity error. Therefore, both powertrain configurations could be used for the final HEV. The blue shaded areas of Fig. 7-Fig. 8 show that the genset is providing full power to the DC-Link during towing operations. The yellow shaded regions in Fig. 7-Fig. 8 show that the genset is providing full power to the DC-Link and the battery pack is being charged. Since the SOE of the battery packs do not exceed the upper or lower limits, the SOE profiles are deemed acceptable for this duty cycle. A comparison between the electrical energy required and the fuel consumed for both HEV configurations against the original ICE powered vehicle is shown in Table 5.

Table 4 Battery pack parameters used in the pushback HEV for both configuration 1 and configuration 2

Parameter	Value
Per cell	
Rated current capacity (Ah)	66
Rated power capacity (kWh)	3.5
Nominal voltage (V)	52
Continuous power output (kW)	6.5
Peak power output (kW)	12.5
Pack configuration and parameters	
Cells in series per string	12
Strings of series in parallel	2
Upper SOE limit (%)	95
Lower SOE limit (%)	30
Battery pack capacity (kWh)	82
Genset parameters	
Genset power (kW)	86
Genset fuel consumption (L/h)	24

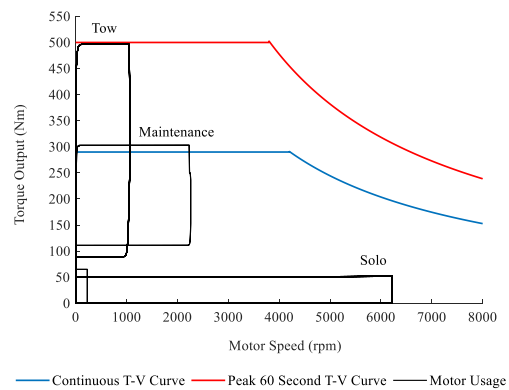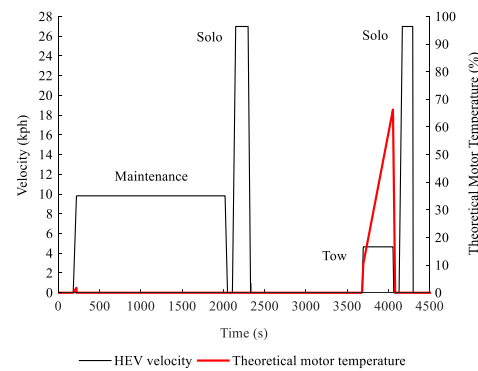**Fig. 4** Motor usage for the HEV with configuration 1 over the daily duty cycle

Fig. 5 Theoretical temperature profile of the traction motors for configuration 1 over a section of the daily duty cycle; 1 maintenance operation, 1 pushback operation and 2 solo runs
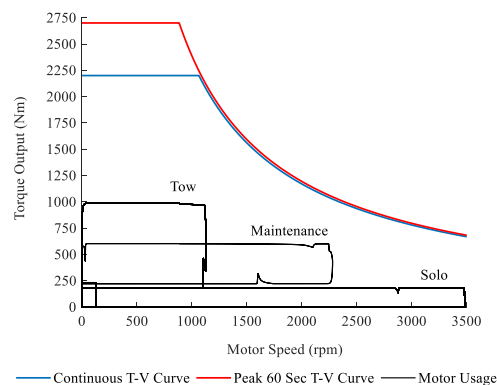

Fig. 6 Motor usage for the HEV with configuration 2 over the daily duty cycle

Table 5 Aeroplane pushback vehicle powertrain configuration and fuel consumption comparison

Powertrain Configuration	Energy required (kWh)	Fuel consumed (L)
ICE	-	190
HEV Configuration 1	244	86.3
HEV Configuration 2	261	91.22

Configuration 2 requires 6.97% more energy and consumes 5.7% more fuel than configuration 1. This is because the dual hub traction motors operate in the higher efficiency overcurrent region for large portions of the duty cycle. However, since configuration 1 does not meet the minimum tractive force regulations, configuration 2 will be used as the final design for the HEV pushback vehicle. Table 5 shows that configuration 2 reduced fuel consumption by 52% from the original ICE powered pushback vehicle over the duty cycle. Without knowing the output emission maps of the genset, it was assumed that there would be a similar reduction in output emissions.
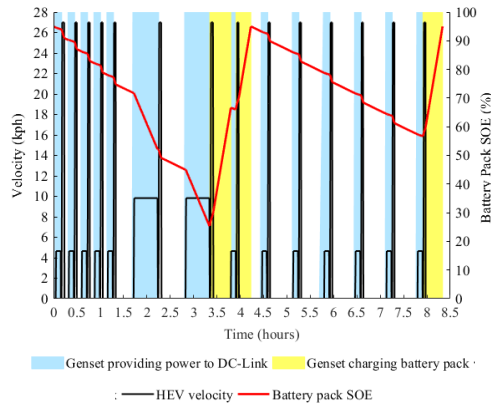

Fig. 7 Velocity profile and battery pack SOE over the complete duty cycle for the HEV using configuration 1
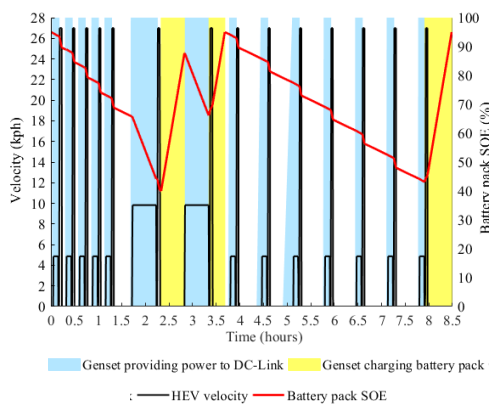

Fig. 8 Velocity profile and battery pack SOE over the complete duty cycle for the HEV using configuration 2

The results of this simulation based sizing strategy have been used in the development of a HEV/EV aeroplane pushback vehicle. A prototype of which is under construction and a future experimental validation of the prediction model is pending, the results of which will be presented in a future publication.

5. Conclusion

This paper has presented a new traction motor sizing strategy for HEV/EVs based on an overcurrent-tolerant prediction model. This model was able to estimate the dynamic and thermal characteristics of a motor operating in the overcurrent region. The intended application of this sizing strategy is during the initial development stages of a HEV/EV to assess the feasibility of prospective traction motors and powertrain configurations. This strategy is applicable to the development of any passenger or heavy duty off-road HEV/EV. A case study was explored where an aeroplane pushback vehicle was converted into a series HEV using this sizing strategy. Two possible HEV configurations using different traction motors and powertrain configurations were then analysed. The advantages of operating in the overcurrent region and its effect on the HEV/EVs driving range, fuel consumption and emissions was revealed. The traction motors operating in the overcurrent region showed to reduce the total energy required and fuel consumed over a rigorous duty cycle. The final HEV design showed a reduction in fuel consumption and engine emissions of 52% from the conventional ICE powered vehicle.

6. Acknowledgements

7. References

[1] T. Hutchinson, S. Burgess and G. Herrmann, "Current hybrid-electric powertrain architectures: applying empirical design data to life cycle assessment and whole-life cost analysis," *Applied Energy,* vol. 119, no. 1, pp. 314-329, 2014.

[2] M. A. Mallouh, E. Abdelhafez, M. Salah, M. Hamdan, B. Surgenor and M. Youssef, "Model development and analysis of a mid-sized hybrid fuel cell/battery vehicle with a representative driving cycle," *Journal of Power Sources,* vol. 260, pp. 62-71, 2014.

[3] A. Castaings, W. Lhomme, R. Trigui and A. Bouscayrol, "Comparison of energy management strategies of a battery/supercapacitors system for electric vehicle under real-time constraints," *Applied Energy,* vol. 163, pp. 190-200, 2016.

[4] Q. Zhou, Y. Zhang, Z. Li, J. Li, H. Xu and O. Olatunbosun, "Cyber-Physical Energy-Saving Control for Hybrid Aircraft-Towing Tractor based on Online Swarm Intelligent Programming," *IEEE Transactions on Industrial Informatics,* 2017.

[5] M. Yilmaz, "Limitations/capabilities of electric machine technologies and modelling approaches for electric motor design analysis in plug-in electric vehicle applications," *Renewable and Sustainable Energy Reviews,* pp. 88-99, 2015.

[6] M. Ehsani, A. Ahmadi and D. Fadai, "Modeling of vehicle fuel consumption and carbon dioxide emission in road transport," *Renewable and Sustainable Energy Reviews,* vol. 53, no. 1, pp. 1638-1648, 2016.

[7] M. Ehsani, K. Rahman and H. Toliyat, "Propulsion System Design of Electric and Hybrid Vehicles," *IEEE Transactions on Industrial Electronics,* vol. 44, no. 1, pp. 19-27, 1997.

[8] X. Liu, D. Diallo and C. Marchand, "Design methodology of hybrid electric vehicle energy sources: Application to fuel cell vehicles," *International Journal of Automotive Technology,* vol. 12, no. 3, p. 433−441, 2011.

[9] F. Millo, C. Cubito, L. Rolando, E. Pautasso and E. Servetto, "Design and development of an hybrid light commercial vehicle," *Energy,* vol. 136, pp. 90-99, 2017.

[10] C. C. Chan, "The State of the Art of Electric, Hybrid, and Fuel Cell Vehicles," *Proceedings of the IEEE,* vol. 95, no. 4, pp. 704 - 718, 2007.

[11] A. Emadi, K. Rajashekara, S. Williamson and S. Lukic, "Topological overview of hybrid electric and fuel cell vehicular power system architectures and configurations," vol. 54, no. 3, 2005.

[12] A. Emadi, Y. J. Lee and K. Rajashekara, "Power Electronics and Motor Drives in Electric, Hybrid Electric, and Plug-In Hybrid Electric Vehicles," *IEEE Transactions on Industrial Electronics,* vol. 55, no. 6, pp. 2237 - 2245, 2008.

[13] K. Butler, M. Ehsani and P. Kamath, "A Matlab-Based Modeling and Simulation Package for Electric and Hybrid Electric Vehicle Design," *IEEE Transactions on vehicular technology,* vol. 48, no. 6, pp. 1770-1778, 1998.

[14] G.Offer, D.Howey, M.Contestabile, R.Clague and N.P.Brandon, "Comparative analysis of battery electric, hydrogen fuel cell and hybrid vehicles in a future sustainable road transport system," *Energy Policy,* vol. 38, no. 1, pp. 24-29, 2010.

[15] Q. Zhou, W. Zhang, S. Cash, O. Olatunbosun, HongmingXu and G. Lu, "Intelligent sizing of a series hybrid electric power-train system based on Chaos-enhanced accelerated particle swarm optimization," vol. 189, 2017.

[16] M. Pourabdollah, E. Silvas, N. Murgovski, M. Steinbuch and B. Egardt, "Optimal sizing of a series PHEV: comparison between convex optimization and particle swarm optimization," *IFAC-PapersOnLine,* vol. 48, no. 15, pp. 16-22, 2015.

[17] X. Wu, B. Cao, X. Li, J. Xu and X. Ren, "Component sizing optimization of plug-in hybrid electric vehicles," *Applied Energy,* vol. 88, no. 3, pp. 799-804, 2011.

[18] S. Cash and O. Olatunbosun, "Fuzzy logic field-oriented control of an induction motor and a permanent magnet synchronous motor for hybrid/electric vehicle traction applications," *International Journal of Electric and Hybrid Vehicles,* vol. 9, no. 3, pp. 269-284, 2017.

[19] S. Evangelou and W. Shabbir, "Dynamic modeling platform for series hybrid electric vehicles," *International Federation of Automatic Control,* vol. 49, no. 11, pp. 533-540, 2016.

[20] J. Lemmens, P. Vanassche and J. Driesen, "Optimal Control of Traction Motor Drives Under Electrothermal Constraints," *IEEE Journal of Emerging and Selected Topics in Power Electronics,* vol. 2, no. 2, pp. 249 - 263, 2014.

[21] G. Pellegrino, A. Vagati, B. Boazzo and P. Guglielmi, "Comparison of Induction and PM Synchronous Motor Drives for EV Application Including Design Examples," *IEEE Transactions on Industry Applications,* vol. 48, no. 6, pp. 2322 - 2332, 2012.

[22] P. Mellor, D. Roberts and D. Turner, "Lumped parameter thermal model for electrical machines of TEFC design," *IEE Proceedings B - Electric Power Applications,* vol. 138, no. 5, pp. 205-218, 1991.

[23] P. Zhang, Y. Du, T. G. Habetler and B. Lu, "A Survey of Condition Monitoring and Protection Methods for Medium-Voltage Induction Motors," *IEEE Transactions on Industry Applications,* vol. 47, no. 1, pp. 34-36, 2011.

[24] Z. Gao, T. G. Habetler, R. G. Harley and R. S. Colby, "A Sensorless Adaptive Stator Winding Temperature Estimator for Mains-Fed Induction Machines With Continuous-Operation Periodic Duty Cycles," *IEEE Transactions on Industry Applications,* vol. 44, no. 5, pp. 1533-1542, 2008.

[25] R. Beguenane and M. Benbouzid, "Induction motors thermal monitoring by means of rotor resistance identification," *IEEE Transactions on Energy Conversion,* vol. 14, no. 3, pp. 566 - 570, 1999.

[26] Z. Gao, T. G. Habetler and R. G. Harley, "A Complex Space Vector Approach to Rotor Temperature Estimation for Line-Connected Induction Machines With Impaired Cooling," *IEEE Transactions on Industrial Electronics,* vol. 56, no. 1, pp. 239 - 247, 2009.

[27] R. Babau, I. Boldea, T. J. E. Miller and N. Muntean, "Complete Parameter Identification of Large Induction Machines From No-Load Acceleration–Deceleration Tests," *IEEE Transactions on Industrial Electronics,* vol. 54, no. 4, pp. 1962 - 1972, 2007.

[28] C. Grantham and D. McKinnon, "Rapid parameter determination for induction motor analysis and control," *IEEE Transactions on Industry Applications,* vol. 39, no. 4, pp. 1014 - 1020, 2003.

[29] M. Uddin, T. Radwan and M. Rahman, "Performances of fuzzy-logic-based indirect vector control for induction motor drive," *IEEE Transactions on Industry Applications,* vol. 38, no. 5, pp. 1219-1225, 2002.

[30] T. D. Gillesspie, Fundamentals of Vehicle Dynamics, Warrendale,PA: Society of Automotive Engineers, Inc, 1992.

[31] D. W. Gao, C. Mi and A. Emadi, "Modeling and Simulation of Electric and Hybrid Vehicles," *Proceedings of the IEEE,* vol. 95, no. 4, pp. 729 - 745, 2007.

8. Appendix 1

Table 6 ICE Speed-Torque characteristics

Speed (rpm)	Torque (Nm)
600	595
700	630
900	741
1100	864
1300	987
1500	990
1900	932
2300	915
2500	830

9. Appendix 2

Nomenclature

g	Acceleration of gravity (m.s^{-2})
ρ	Air density (kg.m^{-3})
J_{Batt}	Battery pack energy (J)
F_{Aero}	Force - Aerodynamic drag (Nm)
F_{Brake}	Force - Brake (Nm)
F_{B-max}	Force - Brake maximum (Nm)
$F_{Rolling}$	Force - Rolling resistance (Nm)
$F_{Traction}$	Force - Traction (Nm)
ω_b	Motor - Base speed (rad.s^{-1})
η_e	Motor - Electrical efficiency
P_m	Motor - Electrical power (kW)
ω_m	Motor - Rotor speed (rad.s^{-1})
α	Pedal activation - Accelerator (%)
β	Pedal activation - Brake (%)
P_{Aux}	Power - Auxiliary (kW)
P_{Gen}	Power - Genset output (kW)
P_m	Power - Motor (kW)
I_{Fd}	Rotational inertia - Final drive (kg.m^2)
I_{ICE}	Rotational inertia - Internal combustion engine (kg.m2)
I_m	Rotational inertia - Traction motor (kg.m^2)
I_T	Rotational inertia - Transmission (kg.m2)
I_{Wh}	Rotational inertia - Wheel (kg.m2)
τ_c	Torque output - Continuous (Nm)

τ_{ICE}	Torque output - Internal combustion engine (Nm)
τ_P	Torque output - Overcurrent (Nm)
δ	Torque position
T	Temperature - Estimated (%)
T_{High}	Temperature limit - High (%)
T_{Low}	Temperature limit - Low (%)
TF	Temperature Factor (%)
t	Time (s)
t_{Stop}	Time - Cool-down (s)
t_{Lim}	Time - Overcurrent limit (s)
a_x	Vehicle - Acceleration (m.s^{-2})
C_D	Vehicle - Coefficient of aerodynamic drag
f_r	Vehicle - Coefficient of rolling resistance
M_r	Vehicle - Effective vehicle mass (kg)
η_{fd}	Vehicle - Final drive efficiency
N_{T-fd}	Vehicle - Final drive and transmission ratio combined
N_{fd}	Vehicle - Final drive ratio
A	Vehicle - Frontal area (m^2)
M_{Veh}	Vehicle - Mass (kg)
N_T	Vehicle - Transmission ratio
U	Vehicle - Velocity (m.s^{-1})
r_w	Vehicle - Wheel rolling radius (m)
EV	Electric Vehicle
HEV	Hybrid Electric Vehicle
ICE	Internal Combustion Engine
SOE	State of Energy